DEEP LEARNING BASED PREDICTION OF SUN-INDUCED FLUORESCENCE FROM HYPLANT IMAGERY

Jim Buffat[1], Miguel Pato[2], Kevin Alonso[3], Stefan Auer[2], Emiliano Carmona[2], Stefan Maier[2], Rupert Müller[2], Patrick Rademske[1], Uwe Rascher[1] and Hanno Scharr[4]

[1] Forschungszentrum Jülich GmbH, Institute of Bio- and Geosciences, IBG-2: Plant Sciences, Jülich, Germany
[2] German Aerospace Center (DLR), Earth Observation Center, Remote Sensing Technology Institute, Oberpfaffenhofen, Germany
[3] RHEA Group c/o European Space Agency (ESA), Largo Galileo Galilei, Frascati 00044, Italy
[4] Forschungszentrum Jülich GmbH, Institute of Advanced Simulations, IAS-8: Data Analytics and Machine Learning, Jülich, Germany

ABSTRACT

The retrieval of sun-induced fluorescence (SIF) from hyperspectral imagery is an ill-posed problem that has been tackled in different ways. We present a novel retrieval method combining semi-supervised deep learning with an existing spectral fitting method. A validation study with in-situ SIF measurements shows high sensitivity of the deep learning method to SIF changes even though systematic shifts deteriorate its absolute prediction accuracy. A detailed analysis of diurnal SIF dynamics and SIF prediction in topographically variable terrain highlights the benefits of this deep learning approach.

***Index Terms*—** solar-induced fluorescence, hyperspectral sensors, radiative transfer, machine learning

1. INTRODUCTION

Sun-induced fluorescence (SIF) has gained much attention as an important biophysical parameter over the last decades. Sensor and retrieval method development have set the path to establish spatially contiguous SIF estimates. The close causal link of the SIF signal to the photosynthetic machinery of plants is a valuable tool to infer plant dynamics remotely. Prominent algorithms for SIF retrieval from hyperspectral data, such as the well-established Improved Fraunhofer Line Discrimination (iFLD) [1] and the Spectral Fitting Method (SFM) [2] have been developed and tested notably on HyPlant data [3]. HyPlant is an airborne hyperspectral sensor operated as a test version for the FLORIS sensor of the upcoming spaceborne FLEX mission aiming at SIF retrieval on a global scale [4]. Thus, the development of accurate and versatile SIF estimators for this sensor are a useful step towards fulfilling the ambitious requirements of the FLEX mission.

HyPlant Campaign	FLOX	$\lvert\mathcal{D}\rvert$	Location
SEL-2018 (600m)	✓	172 (12)	Selhausen, DE
WST-2019 (1500m)	✓	53 (16)	Braccagni, IT
NRS-2019 (1500m)	–	27 (12)	Braccagni, IT
TR32-2019 (1800m)	–	66 (8)	Jülich, DE
GLO-2021 (1150m)	✓	88 (7)	Mollerussa, ES
CKA-2022 (350m)	✓	37 (12)	Klein Altendorf, DE

Table 1: Compiled data sets. FLOX: availability of simultaneous FLOX data. $\lvert\mathcal{D}\rvert$: used # patches [$\times 10^3$] (# acquisitons)

2. DATA & METHODS

We present a neural network trained with a novel semi-supervised loss function constructed for SIF retrieval from HyPlant imagery in the O_2A-band. HyPlant is an assembly of two hyperspectral push-broom sensors. The current work makes use of radiometrically calibrated acquisitions in sensor geometry of one of those sensors (FLUO) from the years 2018-2022 as input to a neural network. It covers the range 670 - 780 nm with a spectral sampling of 0.11 nm and a mean FWHM of 0.27 nm [3]. FLUO was designed for SIF retrieval in the O_2A and O_2B bands and is operated on airborne platforms at flight heights varying from 350 m to 1800 m. Tab. 1 lists the data sets used in this work.

The semi-supervised SIF retrieval method presented here does not rely on SIF ground truth, as would be needed for supervised learning. Instead, we use the prediction of SIF (and of other relevant variables) in conjunction with a simulation model reconstructing the signal. The methodology is thus very similar to SFM, hence we'll refer to the network as SFMNN. In SFM a least-squares estimation of model parameters is performed to retrieve fluorescence and reflectance. In contrast to this, we use the objective function minimized in SFM as a loss formulation for training our neural network in a semi-supervised fashion. In the same logic, the same

simulation model as used in SFM has been implemented to promote comparability in a validation study (cf. Sec. 3). This validation study is conducted with in-situ iFLD SIF measurements derived from data acquired by FLOX systems (www.jb-hyperspectral.com). These measurements have a footprint of the order of a square meter allowing to derive high quality SIF estimates as 'ground truth'. We use FLOX SIF estimates within a 60 s window around the overflight time for a perfomance analysis comparing SFMNN to SFM and iFLD SIF estimates from HyPlant imagery.

2.1. Signal Reconstruction

SFMNN is a network trained to decompose and reconstruct HyPlant at-sensor radiance in the spectral range 750 - 761.7 nm. It predicts a set of parameters from a shared encoding for each pixel in patches (17 $\times$ 17 pixels) cropped from the FLUO radiance product. This parameter set is fed into a deterministic four-stream radiative transfer model [5] to evaluate the residual between the reconstructed and measured at-sensor radiance, cf. sim in Fig. 1. In more detail, the signal reconstruction requires spectral functions for the reflectance, fluorescence emission and atmospheric transfer functions. We model the reflectance $R(\lambda)$ as a linear function and the fluorescence $f(\lambda)$ as a Gaussian with fixed mean at 740 nm and fixed standard deviation $\sigma_f = 20$ nm requiring the prediction of a reflectance slope $dR/d\lambda$ and offset $R_{750\text{nm}}$ and a fluorescence amplitude $f_{\text{O}_2\text{A}}$. The atmospheric functions needed for the four-stream model are estimated by first deriving a PCA decomposition over existing estimations of these transfer functions for specific data sets. Since data acquisition of HyPlant is conducted under comparable atmospheric conditions we assume that we can fit new data with parameterizations t_{ATM} lying in the span of this PCA decomposition. The network trained to perform the decomposition task is outlined in Fig. 1. Each of the encoding and decoding modules is a residual network. In the present work we used an input dimension configuration of (100, 100, 50, 50) for the encoder and (100, 50, 50, 50) for all of the decoders. Linear heads were used to cast the decoders outputs to the required parameter dimension. As outlined below, we required constant t_{ATM} over single patches. We realized this by taking mean over the atmospheric decoders' outputs.

2.2. Weighting of the Reconstruction Error

The SIF signal-to-noise ratio increases strongly in the O_2A-band. Accordingly, we weight the reconstruction error by

$$w_\lambda = \left\langle \frac{1}{\sigma_\lambda^2} \frac{\sum_{\lambda'} f_{\lambda'}^2}{\sum_{\lambda'} f_{\lambda'}^2/\sigma_{\lambda'}^2} \right\rangle_{p(L,f)} \tag{1}$$

where we denote f denotes the predicted at-sensor fluorescence, σ_λ the estimated variance of the total at-sensor radiance and $\langle \dots \rangle_{p(L,f)}$ the mean over a fixed distribution

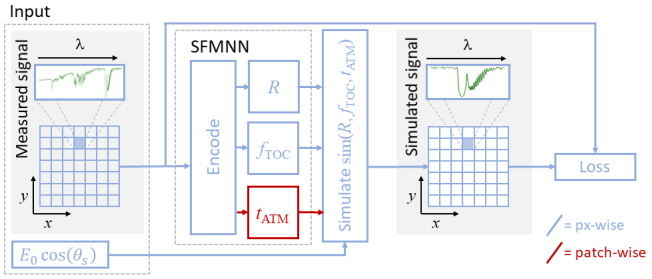

Fig. 1: Outline of SFMNN. R, f_{TOC} and t_{ATM} denote reflectance, top-of-canopy fluorescence and atmosphere parameter groups. E_0 : solar irradiance, θ_s: zenith angle

of at-sensor radiance and fluorescence emission in a simulated HyPlant acquisition line. With this weighting, the Moore-Penrose solution to the linearized retrieval problem with known reflectance constitutes a Best Linear Unbiased Estimator (BLUE).

2.3. Loss and Constraint Formulation

The estimation of the parameterization for reconstruction of at-sensor radiance without ancillary data is an ill-posed problem [6]. Additional constraints are needed to minimize the reconstruction error in a plausible solution space. Additionally to the functional constraints implemented as described above we assume the atmosphere to vary only over distances significantly larger than individual spatial pixels. We implement this architecturally by deriving predictions t_{ATM} over spatial patches of fixed pixel size. Besides these constraints, we included two regularizers in the loss promoting physiological and physical validity. First, we can safely assume to have non-zero SIF only in pixels with NDVI $\geq \tau$. This is a similar constraint as is used in SFM to find a suitable atmospheric parameterization. Accordingly, we set the same threshold $\tau = 0.15$. Secondly, we assume that the diffusive part of the at-sensor radiance is low. Thus, we punish the network if the total atmospheric transfer function $t_{\text{tot}} = L^R\, R^{-1}/E_s^0\, \cos(\theta_s) > 1$, where L^R is the predicted radiance without SIF contribution. R denotes the pixel reflectance and $E_s^0\, \cos(\theta_s)$ the solar irradiance modulated by the solar zenith angle (SZA). In summary, we train our network with the loss

$$\begin{aligned} \ell(y, \hat{y}) &= (\ell_{R,f} + \gamma_f\, \ell_f + \gamma_N\, \ell_{\text{NDVI}} + \gamma_a\, \ell_{\text{atm}})(y,\, \hat{y}) \\ &= \left\langle (y(\lambda) - \hat{y}(\lambda))^2 + \gamma_{\text{f}} \left(w_\lambda\, (y(\lambda) - \hat{y}(\lambda))^2 \right)_{\delta \text{R}=0} \right\rangle_{\lambda \in \mathcal{W}} \\ &\quad + \gamma_{\text{N}}\, \hat{f}\, \delta\,(\text{NDVI}_y \geq t) + \gamma_{\text{a}}\, \text{ReLU}(\hat{t}_{\text{tot}} - 1) \end{aligned} \tag{2}$$

for measured and predicted spectra y and $\hat{y}$ in the spectral range $\mathcal{W}$. The brackets denote the mean over the spectral window $\mathcal{W}$, $\delta R = 0$ a term that doesn't contribute to the gradient of network weights of R and δ denotes a Boolean. We set throughout all experiments $\gamma_{\text{f}} = 5$, $\gamma_{\text{N}} = 1$, $\gamma_{\text{a}} = 1$ and $\mathcal{W}$ = [750, 761.7] nm.

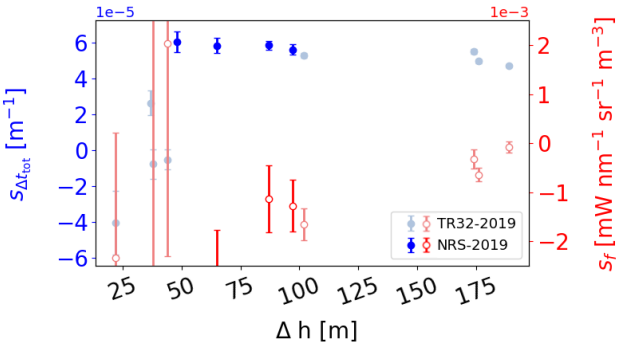

Fig. 2: Slopes $s_{\Delta t_{\mathrm{tot}}}$ (filled, left) and s_f (open, right) of the marginal distribution $p(\Delta t_{\mathrm{tot}}|\Delta h)$ and $p(f|\Delta h)$. Each data point represents a single acquisition.

3. RESULTS & DISCUSSION

3.1. Training Set-up

The data sets on which we base the following analysis were compiled from the campaign data sets listed in Tab. 1. We selected subsets of the data guided by the principle to cover a wide range of observational conditions and close temporal matches with ground-based FLOX measurements for validation.

The PCA decomposition used to model the atmospheric transfer functions in the simulation model was computed from MODTRAN generated atmospheric functions for several data subsets from 2018 and 2019 taken at different flight heights. These atmospheric functions are estimated as a side-product when predicting SIF with the SFM baseline.

3.2. Comparison with in-situ SIF measurements

In order to validate the SIF prediction accuracy of SFMNN, we make use of the FLOX derived SIF measurements. Tab. 2 shows the performance of SFMNN predictions along with the iFLD and SFM baseline methods. We compute the Pearson correlation r_{pear}, R^2 scores and the mean absolute error (MAE) between the HyPlant and FLOX derived SIF estimates. R^2 is understood to be computed on HyPlant derived SIF estimates that were linearly calibrated to $\mathrm{SIF}_{\mathrm{FLOX}}$ such that the influence of systematic biases and under- and over-estimations were excluded from this metric. The linear calibration was derived as the mean of a cross-validation over subsets of the data sets.

It can be observed that the relative SIF variation of SFMNN, as expressed by R^2 and r_{pear}, is on par with the baselines. On the other hand, mean absolute errors (MAE) are in almost all cases significantly larger than for SFM. This is due to systematic shifts in the prediction of individual acquisitions. We show this by listing the performance results for SFMNN under a calibration with SFM SIF predictions. In the columns with subscript c we list the results for SFMNN SIF predictions linearly calibrated to SFM SIF per flight line by fitting linearly the SFM-SFMNN prediction distribution. This calibration greatly decreases the MAE in all cases where SFMNN underperformed, though consistency as measured by r_{pear} is not guaranteed to be stable.

Data Set		r^{pear}	r_c^{pear}	R^2	R_c^2	MAE	MAE$_c$	N
SEL 2018	SFM	0.91		0.83		0.87		10
	SFMNN	**0.96**	0.95	**0.91**	**0.91**	**0.62**	0.71	10
	iFLD	0.81		0.65		0.65		10
WST 2019	SFM	-0.47		0.22		0.53		21
	SFMNN	**0.51**	-0.18*	0.26	0.03	0.81	**0.44**	21
	iFLD	-0.63		**0.39**		4.88		21
GLO 2021	SFM	**0.98**		**0.97**		0.34		5
	SFMNN	0.95	0.97	0.91	0.92	0.50	**0.12**	5
	iFLD	0.88		0.77		0.79		5
CKA 2022	SFM	0.63*		0.39		**0.38**		6
	SFMNN	0.76*	**0.84**	0.57	**0.69**	0.51	0.40	6
	iFLD	-0.63*		-2.10		1.17		4

Table 2: FLOX derived SIF measurements compared to SFMNN, SFM and iFLD SIF predictions. r_{pear} maked with * have $p > 0.05$. MAE is given in units of mW nm^{-1}m^{-2} sr^{-1}.

3.3. Height dependent O_2A-band variation

In order to evaluate whether SFMNN can be applied in topographically variable terrain, we test its ability to disentangle the atmospheric transfer from fluorescence and reflectance there. Variable topography impacts the O_2A-band depth as the distance through air changes. The baseline SFM explains this change in O_2A-band depth by a change in SIF. In order to investigate the behaviour of SFMNN under strong O_2A-band depth changes we train SFMNN on the NRS-2019 and TR32-2019 data sets that comprise acquisitions with strong elevation changes Δh. In order to avoid issues in the early phases of training that can arise with these data sets, we warm start the training from the WST-2019 network used in Sec. 3.2. Only acquisitions around noon were included in this analysis to exclude low incidence angles that induce large variance due to simultaneous presence of sun-facing and shadowed hill slopes. We highlight that non-homogeneous surface conditions (i.e. vegetative cover) across the height changes can introduce non-topography related variance such that we expect the clearest results in flight lines with the largest height change.

In Fig. 2 we show the slope of linear fits to the marginal distributions $p(\Delta t_{\mathrm{tot}}|\Delta h)$ and $p(f|\Delta h)$, where $\Delta t_{\mathrm{tot}} = \min t_{\mathrm{tot}} / \max t_{\mathrm{tot}}$ denotes the band depth. We observe from small s_f that SFMNN is able to produce approximately constant SIF distributions over varying topography. It does so by changing the atmospheric transfer functions accordingly at a rate which is constant across different data sets as can be seen from the approximately constant $s_{\Delta t_{\mathrm{tot}}}$. Thus, Fig. 2 suggests

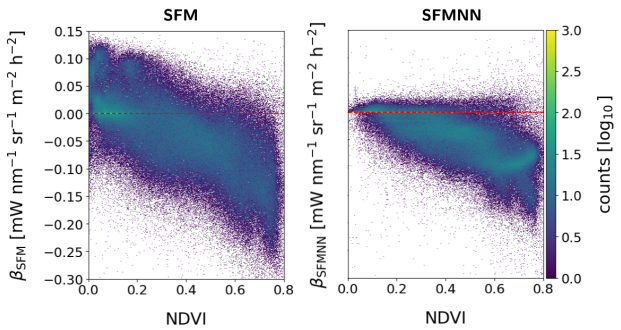

Fig. 3: NDVI-β distributions for SFM (left) and SFMNN (right), where β denotes the second order derivative of the time series per pixel.

that SFMNN is able to consistently predict O_2A-band depth variation with height. This effect is most pronounced in flight lines with the largest $\Delta h > 50$ m where the topographic effect on the O_2A-band depth is most important.

3.4. Diurnal Variation

In order to evaluate the predicted time dynamics of SIF we trained and evaluated a network on the WST-2019 data set. A subset of the flight lines in this data set constituted a time series sampling a whole day (19/06/2023) with 9 repeated acquisitions covering approximately the same footprint. We subsequently fitted second order polynomials to coregistered pixel predictions forming time series and used its second order derivative β as a measure of SIF variability over the course of the day. In Fig. 3 we compare a spatial pixels mean NDVI value with β derived from SFM (left) and SFMNN (right) predictions. The NDVI-β distributions coincide well for pixels with NDVI > 0.6. An upper limit $\beta_{\mathrm{SFMNN}} < 0$ can be observed in Fig. 3 which is not present in the SFM predictions. This upper limit is to be expected from a physiological argument as we expect SIF to peak around noon and to vanish in the morning and evening. Equally, an increasing absolute value of β with NDVI can be motivated physiologically. Clearly, the semi-supervised training has allowed SFMNN to learn internal representations respecting this constraint.

4. CONCLUSION & OUTLOOK

This work has shown that SFMNN achieved on par performance to baseline methods in terms of predicting relative SIF variation. SFMNN could be shown to be consistently sensitive to SIF changes present in in-situ measurements. However, SFMNN did not outperform SFM in terms of absolute SIF estimation. Good performance of SFMNN under linear calibration per acquisition with SFM statistics in almost all cases has highlighted that SFMNN is suffering from systematic shifts. Analysis regarding the adaptivity of the atmospheric prediction and diurnal SIF dynamics highlighted the benefits of using a neural network with physically motivated constraint formulation for SIF retrieval. SFMNNs higher consistency is a valuable contribution to improving SIF estimation from HyPlant imagery and offers the potential to be applied to other hyperspectral data sources in a straightforward manner. A more complete analysis and discussion of possibilities to reduce the need for calibration is currently being prepared.

Acknowledgement: This work is funded by the Helmholtz Initiative and Networking Fund, Helmholtz AI, Deutsches Zentrum für Luft- und Raumfahrt and Forschungszentrum Jülich GmbH. The authors gratefully acknowledge the computing time granted by the JARA Vergabegremium and provided on the JARA Partition part of the supercomputer JURECA [7] at Forschungszentrum Jülich.

5. REFERENCES

[1] L. Alonso *et al.*, "Improved Fraunhofer Line Discrimination Method for Vegetation Fluorescence Quantification," *IEEE Geoscience and Remote Sensing Letters*, vol. 5, no. 4, pp. 620–624, Oct. 2008.

[2] S. Cogliati *et al.*, "A Spectral Fitting Algorithm to Retrieve the Fluorescence Spectrum from Canopy Radiance," *Remote Sensing*, vol. 11, no. 16, p. 1840, Jan. 2019.

[3] B. Siegmann *et al.*, "The High-Performance Airborne Imaging Spectrometer HyPlant—From Raw Images to Top-of-Canopy Reflectance and Fluorescence Products: Introduction of an Automatized Processing Chain," *Remote Sensing*, vol. 11, no. 23, p. 2760, Jan. 2019.

[4] M. Drusch *et al.*, "The fluorescence explorer mission concept—esa's earth explorer 8," *IEEE Transactions on Geoscience and Remote Sensing*, vol. 55, no. 3, pp. 1273–1284, 2017.

[5] W. Verhoef *et al.*, "Simulation of Sentinel-3 images by four-stream surface–atmosphere radiative transfer modeling in the optical and thermal domains," *Remote Sensing of Environment*, vol. 120, pp. 197–207, May 2012.

[6] C. Frankenberg *et al.*, "Disentangling chlorophyll fluorescence from atmospheric scattering effects in O2 A-band spectra of reflected sun-light," *Geophysical Research Letters*, vol. 38, no. 3, 2011.

[7] Jülich Supercomputing Centre, "JURECA: Data Centric and Booster Modules implementing the Modular Supercomputing Architecture at Jülich Supercomputing Centre," *Journal of large-scale research facilities*, vol. 7, no. A182, 2021. [Online]. Available: http://dx.doi.org/10.17815/jlsrf-7-182